

Robust MRI Reconstruction by Smoothed Unrolling (SMUG)

Shijun Liang, *Student Member, IEEE*, Van Hoang Minh Nguyen, Jinghan Jia, *Student Member, IEEE*, Ismail Alkhouri, *Member, IEEE*, Sijia Liu, *Senior Member, IEEE*, Saiprasad Ravishankar, *Senior Member, IEEE*

Abstract—As the popularity of deep learning (DL) in the field of magnetic resonance imaging (MRI) continues to rise, recent research has indicated that DL-based MRI reconstruction models might be excessively sensitive to minor input disturbances, including worst-case additive perturbations. This sensitivity often leads to unstable, aliased images. This raises the question of how to devise DL techniques for MRI reconstruction that can be robust to train-test variations. To address this problem, we propose a novel image reconstruction framework, termed **SMOOTHED UNROLLING (SMUG)**, which advances a deep unrolling-based MRI reconstruction model using a randomized smoothing (RS)-based robust learning approach. RS, which improves the tolerance of a model against input noises, has been widely used in the design of adversarial defense approaches for image classification tasks. Yet, we find that the conventional design that applies RS to the entire DL-based MRI model is ineffective. In this paper, we show that SMUG and its variants address the above issue by customizing the RS process based on the unrolling architecture of a DL-based MRI reconstruction model. Compared to the vanilla RS approach, we show that SMUG improves the robustness of MRI reconstruction with respect to a diverse set of instability sources, including worst-case and random noise perturbations to input measurements, varying measurement sampling rates, and different numbers of unrolling steps. Furthermore, we theoretically analyze the robustness of our method in the presence of perturbations. Our code is available at https://github.com/sjames40/SMUG_journal.

Index Terms—Magnetic resonance imaging, machine learning, deep unrolling, robustness, randomized smoothing, compressed sensing.

I. INTRODUCTION

Magnetic resonance imaging (MRI) is a popular noninvasive imaging modality, which involves sequential and slow data collection. As such, MRI scans can be accelerated by collecting limited data. In this case, the process of image reconstruction requires tackling an ill-posed inverse problem. To deliver accurate image reconstructions from such limited information, compressed sensing (CS) [1] has been extensively used. Conventional CS-MRI assumes the underlying image’s sparsity (in practice, enforced in the wavelet domain [2] or via total variation [3]). As further improvement to conventional CS, various learned sparse signal models have been well-studied,

such as involving patch-based synthesis dictionaries [4], [5], or sparsifying transforms [6], [7]. Learned transforms have been shown to offer an efficient and effective framework for sparse modeling in MRI [8].

Due to the outstanding representation power of convolutional neural networks (CNNs), they have been applied in single-modality medical imaging synthesis in recent years [9]–[12]. The U-net neural network, presented in [13] and referenced in numerous studies, is a popular deep CNN for many tasks involving image processing. They exhibit two key features: the use of a diminishing path for gathering contextual information, and a symmetric expansion path in the U-net for precise localization.

Hybrid-domain DL-based image reconstruction methods, such as **Model-based reconstruction using Deep Learned priors (MODL)** [11], are used to enhance stability and performance by ensuring data consistency in the training and reconstruction phases. In MR imaging, data consistency layers are often essential in reconstruction networks to ensure the image agrees with the measurements model [14], [15]. Various methods such as [16], [17] maintain this consistency by deep unrolling-based architectures, which mimic a traditional iterative algorithm and learn the associated regularization parameters. Other approaches ensure data consistency by applying methods such as denoising regularization [18] and plug-and-play techniques [19]. Despite their recent advancements, DL-based MRI reconstruction models are shown to be vulnerable to tiny changes in the input, shifts in the measurement sampling rate [20], [21], and varying iteration numbers in unrolling schemes [22]. In such cases, the resulting images from DL models are of inferior quality which could possibly lead to inaccurate diagnoses and, consequently, undesirable clinical consequences.

It is of much importance in medical imaging applications to learn reconstruction models that are robust to various measurement artifacts and noise, or scan or data variations at test time. Although there exist numerous robustification techniques [23]–[26] to tackle the instability of DL models in image classification tasks, methods to enhance the robustness of DL-based MRI reconstruction models are less explored due to their regression-based learning targets. Methods such as randomized smoothing (RS) and its variations [25]–[27], are often used in image classification. They diverge from traditional defense methods [23], [24] such as adversarial training, which provide some empirical robustness but are computationally expensive and could fail under more diverse perturbations. RS ensures the model’s stability within a radius surrounding the input image [25], which could be critical for medical use cases such as MRI. Recent early-stage research has begun to apply RS to

S. Liang (corresponding author: liangs16@msu.edu) is with the Biomedical Engineering (BME) Department at Michigan State University (MSU), East Lansing, MI, 48824, USA. J.Jia (jjajingh@msu.edu) is with the Computer Science and Engineering (CSE) Department at MSU. M. Nguyen (nguye954@msu.edu) is with the Mathematics Department at MSU. I. Alkhouri (alkhour3@msu.edu & ismailal@umich.edu) is with the Computational Mathematics, Science & Engineering (CMSE) Department at MSU and a visiting scholar in the Electrical Engineering & Computer Science Department at the University of Michigan, Ann Arbor, MI, 48109, USA. S. Liu (liusij15@msu.edu) is with the CSE Department at MSU. S. Ravishankar (ravisha3@msu.edu) is with the CMSE & BME Departments at MSU.

DL-based MRI reconstruction in an end-to-end manner [28]. However, the end-to-end RS approach might not always be an appropriate fit for all image reconstructors, such as physics-based and hybrid methods.

In our recent conference work [29], we proposed integrating the RS approach within the MODL framework for the problem of MR image reconstruction. This is accomplished by using RS in each unrolling step and at the intermediate unrolled denoisers in MODL. This strategy is underpinned by the ‘pre-training + fine-tuning’ technique [26], [30]. In [29], we empirically showed that this approach is effective. In this paper, we provide an analysis and conditions under which the proposed smoothed unrolling (SMUG) technique is robust against perturbations. Furthermore, we introduce a novel weighted smoothed unrolling scheme that learns image-wise weights during smoothing unlike conventional RS. This approach improves the reconstruction performance. In this work, we evaluate worst-case additive perturbations in k-space, in contrast to [29], where image-space perturbations were considered. Moreover, this paper includes additional comprehensive experimental results.

A. Contributions

The main contributions of this work are as follows:

- We propose SMUG that systematically integrates RS within a deep unrolled procedure (MODL).
- We provide a theoretical analysis to demonstrate the robustness of SMUG.
- We enhance the performance of SMUG by introducing weighted smoothing as an improvement over conventional RS and showcase the resulting gain.
- We compare our methods with the vanilla MODL [11] and end-to-end RS [28]. Extensive experiments demonstrate the significant improvement of our approach against various types of reconstruction instabilities.

B. Paper Organization

The remainder of the paper is organized as follows. In Section II, we present preliminaries and the problem statement. Our proposed method is described in Section III. Section IV presents experimental results and comparisons, and we conclude in Section V.

II. PRELIMINARIES AND PROBLEM STATEMENT

Setup of MRI reconstruction. Many medical imaging approaches involve ill-posed inverse problems such as the work in [31], where the aim is to reconstruct the original signal $\mathbf{x} \in \mathbb{C}^q$ (vectorized image) from undersampled k-space (Fourier domain) measurements $\mathbf{y} \in \mathbb{C}^p$ with $p < q$. The imaging system in MRI can be modeled as a linear system $\mathbf{y} \approx \mathbf{A}\mathbf{x}$, where \mathbf{A} may take on different forms for single-coil or parallel (multi-coil) MRI, etc. For example, in the single coil Cartesian MRI acquisition setting, $\mathbf{A} = \mathbf{M}\mathbf{F}$, where \mathbf{F} is the 2D discrete Fourier transform and \mathbf{M} is a masking operator that implements undersampling. With the linear observation model, MRI reconstruction is often formulated as

$$\hat{\mathbf{x}} = \arg \min_{\mathbf{x}} \|\mathbf{A}\mathbf{x} - \mathbf{y}\|_2^2 + \lambda \mathcal{R}(\mathbf{x}), \quad (1)$$

where $\mathcal{R}(\cdot)$ is a regularization function (e.g., ℓ_1 norm in the wavelet domain to impose a sparsity prior), and $\lambda > 0$ is the regularization parameter.

MODL [32] is a recent popular supervised deep learning approach inspired by the MR image reconstruction optimization problem in (1). MODL combines a denoising network with a data-consistency (DC) module in each iteration of an unrolled architecture. In MODL, the hand-crafted regularizer, \mathcal{R} , is replaced by a learned network-based prior $\|\mathbf{x} - \mathcal{D}_\theta(\mathbf{x})\|_2^2$ involving a network \mathcal{D}_θ . MODL attempts to optimize this loss by initializing $\mathbf{x}^0 = \mathbf{A}^H \mathbf{y}$, and then iterating the following process for a number of unrolling steps indexed by $n \in \{0, \dots, N-1\}$. Specifically, MODL iterations are given by

$$\mathbf{x}^{n+1} = \arg \min_{\mathbf{x}} \|\mathbf{A}\mathbf{x} - \mathbf{y}\|_2^2 + \lambda \|\mathbf{x} - \mathcal{D}_\theta(\mathbf{x}^n)\|_2^2. \quad (2)$$

After N iterations, we denote the final output of MODL as $\mathbf{x}^N = \mathbf{F}_{\text{MODL}}(\mathbf{x}^0)$. The weights of the denoiser are shared across the N blocks and are learned in an end-to-end supervised manner [11].

Motivation: Lack of robustness in MODL. In [20], it was demonstrated that deep learning-based MRI reconstruction can exhibit instability, when confronted with subtle, nearly imperceptible input perturbations. These perturbations are commonly referred to as ‘adversarial perturbations’ and have been extensively investigated in the context of DL-based image classification tasks, as outlined in [33]. In the context of MRI, these perturbations represent the worst-case additive perturbations, which may be used to evaluate method sensitivity and robustness [20], [34]. Let δ denote a small perturbation of the measurements that falls in an ℓ_∞ ball of radius ϵ , i.e., $\|\delta\|_\infty \leq \epsilon$. Adversarial disturbances then correspond to the worst-case input perturbation vector δ that maximizes the reconstruction error, i.e.,

$$\max_{\|\delta\|_\infty \leq \epsilon} \|\mathbf{F}_{\text{MODL}}(\mathbf{A}^H(\mathbf{y} + \delta)) - \mathbf{t}\|_2^2, \quad (3)$$

where \mathbf{t} is a ground truth target image from the training set (i.e., label). The operator \mathbf{A}^H transforms the measurements \mathbf{y} to the image domain, and $\mathbf{A}^H \mathbf{y}$ is the input (aliased) image to the reconstruction model. The optimization problem in (3) can be effectively solved using the iterative projected gradient descent (PGD) method [23].

In **Fig. 1-(a)** and **(b)**, we show reconstructed images using MODL originating from a benign (i.e., undisturbed) input and a PGD scheme-perturbed input, respectively. It is evident that the worst-case input disturbance significantly deteriorates the quality of the reconstructed image. While one focus of this work is to enhance robustness against input perturbations, **Fig. 1-(c)** and **(d)** highlight two additional potential sources of instability that the reconstructor (MODL) can encounter during testing: variations in the measurement sampling rate (resulting in ‘perturbations’ to the sparsity of the sampling mask in \mathbf{A}) [20] and changes in the number of unrolling steps [22]. In scenarios where the sampling mask (**Fig. 1-(c)**) or number of unrolling steps (**Fig. 1-(d)**) deviate from the settings used during MODL training, we observe a significant degradation in performance compared to the original setup

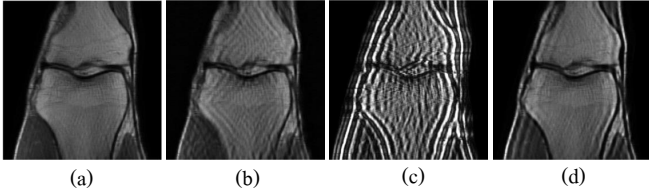


Fig. 1: MODL’s instabilities resulting from perturbations to input data, the measurement sampling rate, and the number of unrolling steps used at testing phase shown on an image from the `fastMRI` dataset [35]. We refer readers to Section IV for further details about the experimental settings. (a) MODL reconstruction from benign (*i.e.*, without additional noise/perturbation) measurements with $4\times$ acceleration (*i.e.*, 25% sampling rate) and 8 unrolling steps. (b) MODL reconstruction from disturbed input with perturbation strength $\epsilon = 0.02$ (see Section IV-A) with other settings identical to (a). (c) MODL reconstruction from clean measurements with $2\times$ acceleration (*i.e.*, 50% sampling), and using 8 unrolling steps. (d) MODL reconstruction from clean or unperturbed measurements with $4\times$ acceleration and 16 unrolling steps.

(**Fig.1-(a)**), even in the absence of additive measurement perturbations. In Section IV, we demonstrate how our method improves the reconstruction robustness in the presence of different types of perturbations, including those in **Fig.1**.

Randomized smoothing (RS). Randomized Smoothing, introduced in [25], enhances the robustness of DL models against noisy inputs. It is implemented by generating multiple randomly modified versions of the input data and subsequently calculating an averaged output from this diverse set of inputs.

Given some function $f(\mathbf{x})$, RS formally replaces f with a smoothed version

$$g(\mathbf{x}) := \mathbb{E}_{\boldsymbol{\eta} \sim \mathcal{N}(\mathbf{0}, \sigma^2 \mathbf{I})} [f(\mathbf{x} + \boldsymbol{\eta})], \quad (4)$$

where $\mathcal{N}(\mathbf{0}, \sigma^2 \mathbf{I})$ denotes a Gaussian distribution with zero mean and element-wise variance σ^2 , and \mathbf{I} denotes the identity matrix of appropriate size. Prior research has shown that RS has been effective as an adversarial defense approach in DL-based image classification tasks [25], [26], [36]. However, the question of whether RS can significantly improve the robustness of MODL and other image reconstructors has not been thoroughly explored. A preliminary investigation in this area was conducted by [28], which demonstrated the integration of RS into MR image reconstruction in an end-to-end (E2E) setting. We can formulate image reconstruction using RS-E2E as

$$\mathbf{x}_{\text{RS-E2E}} = \mathbb{E}_{\boldsymbol{\eta} \sim \mathcal{N}(\mathbf{0}, \sigma^2 \mathbf{I})} [\mathbf{F}_{\text{MODL}}(\mathbf{A}^H \mathbf{y} + \boldsymbol{\eta})]. \quad (\text{RS-E2E})$$

Note that this formulation is a slight modification to the one used in [28], where the random noise vector $\boldsymbol{\eta}$ is directly added to \mathbf{y} . Here, it is added in the image domain (complex-valued) to $\mathbf{A}^H \mathbf{y}$, which is used both as input to MODL and within each data-consistency step in MODL. We found that this approach is slightly better in practice.

Fig. 2 shows a block diagram of RS-E2E-backed MODL. This RS-integrated MODL is trained with supervision in the

standard manner. Although RS-E2E represents a straightforward application of RS to MODL, it remains unclear if the formulation in (RS-E2E) is the most effective method to incorporate RS into unrolled algorithms such as MODL, considering the latter’s specialties, *e.g.*, the involved denoising and the data-consistency (DC) steps.

As such, for the rest of the paper, we focus on studying the following questions **(Q1)–(Q4)**.

(Q1): How should RS be integrated into an unrolled algorithm such as MODL?

(Q2): How do we learn the network $\mathcal{D}_\theta(\cdot)$ in the presence of RS operations?

(Q3): Can we prove the robustness of SMUG in the presence of data perturbations?

(Q4): Can we further improve the RS operation in SMUG for enhanced image quality or sharpness?

III. METHODOLOGY

In this section, we address questions **(Q1)–(Q4)** by taking the unrolling characteristics of MODL into the design of an RS-based MRI reconstruction. The proposed novel integration of RS with MODL is termed SMOOTHED UNROLLING (SMUG). We also explore an extension to SMUG.

A. Solution to **(Q1)**: RS at intermediate unrolled denoisers

As illustrated in **Fig. 2**, the RS operation in RS-E2E is typically applied to MODL in an end-to-end manner. This does not shed light on which component of MODL needs to be made more robust. Here, we explore integrating RS at each intermediate unrolling step of MODL. In this subsection, we present SMUG, which applies RS to the denoising network. This seemingly simple modification is related to a robustness certification technique known as “denoised smoothing” [26]. In this technique, a smoothed denoiser is used, proving to be sufficient for establishing robustness in the model. We use \mathbf{x}_S^n to capture the n -th iteration of SMUG. Starting from $\mathbf{x}_S^0 = \mathbf{A}^H \mathbf{y}$, the procedure is given by

$$\mathbf{x}_S^{n+1} = \arg \min_{\mathbf{x}} \|\mathbf{A}\mathbf{x} - \mathbf{y}\|_2^2 + \lambda \|\mathbf{x} - \mathbb{E}_\eta [\mathcal{D}_\theta(\mathbf{x}_S^n + \boldsymbol{\eta})]\|_2^2, \quad (5)$$

where $\boldsymbol{\eta}$ is drawn from $\mathcal{N}(\mathbf{0}, \sigma^2 \mathbf{I})$. After $N - 1$ iterations, the final output of SMUG is denoted by $\mathbf{x}_S^N = \mathbf{F}_{\text{SMUG}}(\mathbf{x}^0)$. **Fig. 3** presents the architecture of SMUG.

B. Solution to **(Q2)**: SMUG’s pre-training & fine-tuning

In this subsection, we develop the training scheme of SMUG. Inspired by the currently celebrated “pre-training + fine-tuning” technique [26], [30], we propose to train SMUG following this learning paradigm. Our rationale is that pre-training can provide a robustness-aware initialization of the DL-based denoising network for fine-tuning. To pre-train the denoising network \mathcal{D}_θ , we consider a mean squared error (MSE) loss that measures the Euclidean distance between images denoised by \mathcal{D}_θ and the target images, denoted by \mathbf{t} . This leads to the **pre-training** step:

$$\boldsymbol{\theta}_{\text{pre}} = \arg \min_{\boldsymbol{\theta}} \mathbb{E}_{\mathbf{t} \in \mathcal{T}} [\mathbb{E}_\eta \|\mathcal{D}_\theta(\mathbf{t} + \boldsymbol{\eta}) - \mathbf{t}\|_2^2], \quad (6)$$

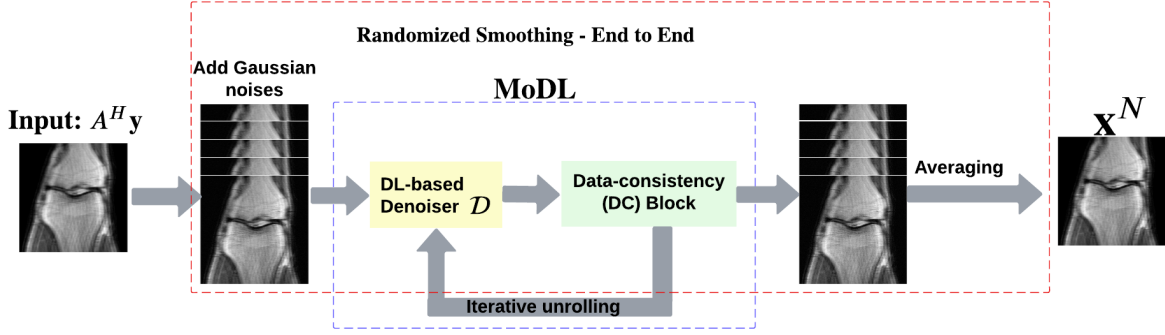


Fig. 2: A schematic overview of RS-E2E.

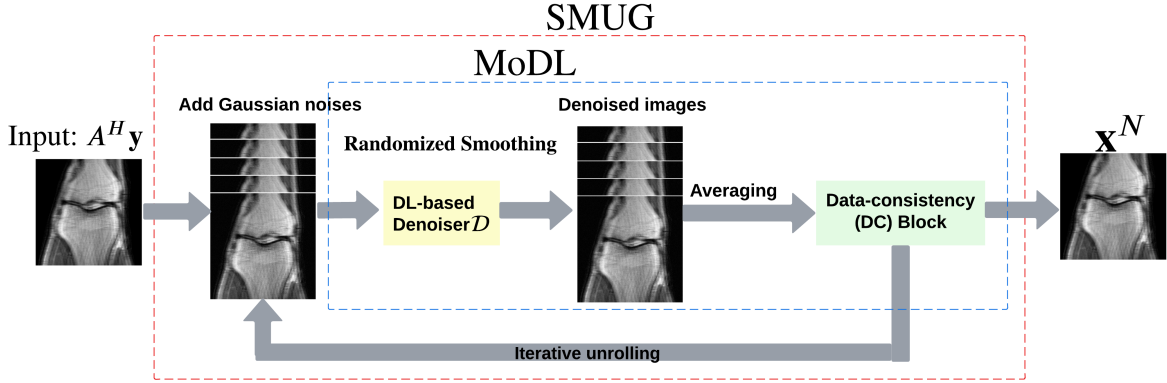


Fig. 3: Architecture of SMUG.

where \mathcal{T} is the set of ground truth images in the training dataset. Next, we develop the fine-tuning scheme to improve θ_{pre} based on the labeled/paired MRI dataset. Since RS in SMUG (Fig. 3) is applied to every unrolling step, we propose an *unrolled stability (UStab)* loss for fine-tuning \mathcal{D}_θ :

$$\ell_{\text{UStab}}(\theta; \mathbf{y}, \mathbf{t}) = \sum_{n=0}^{N-1} \mathbb{E}_\eta \|\mathcal{D}_\theta(\mathbf{x}^n + \eta) - \mathcal{D}_\theta(\mathbf{t})\|_2^2. \quad (7)$$

The UStab loss in (7) relies on the target images, bringing in a key benefit: the denoising stability is guided by the reconstruction accuracy of the ground-truth image, yielding a graceful trade-off between robustness and accuracy.

Integrating the UStab loss, defined in (7), with the standard reconstruction loss, we obtain the **fine-tuned** θ by minimizing $\mathbb{E}_{(\mathbf{y}, \mathbf{t})}[\ell(\theta; \mathbf{y}, \mathbf{t})]$, where

$$\ell(\theta; \mathbf{y}, \mathbf{t}) = \ell_{\text{UStab}}(\theta; \mathbf{y}, \mathbf{t}) + \lambda_\ell \|\mathbf{F}_{\text{SMUG}}(\mathbf{A}^H \mathbf{y}) - \mathbf{t}\|_2^2, \quad (8)$$

with $\lambda_\ell > 0$ is a regularization parameter to strike a balance between the reconstruction error (for accuracy) and the denoising stability (for robustness) terms. We initialize θ as θ_{pre} when optimizing (8) using standard optimizers such as Adam [37].

C. Answer to (Q3): Analyzing the robustness of SMUG in the presence of data perturbations

The following theorem discusses the robustness (i.e., sensitivity to input perturbations) achieved with SMUG. Note that all norms on vectors (resp. matrices) denote the ℓ_2 norm (resp. spectral norm) unless indicated otherwise.

Theorem 1. Assume the denoiser network's output is bounded in norm. Given the initial input image $\mathbf{A}^H \mathbf{y}$ obtained from measurements \mathbf{y} , let the SMUG reconstructed image at the n -th unrolling step be $\mathbf{x}_S^n(\mathbf{A}^H \mathbf{y})$ with RS variance of σ^2 . Let δ denote an additive perturbation to the measurements \mathbf{y} . Then,

$$\|\mathbf{x}_S^n(\mathbf{A}^H \mathbf{y}) - \mathbf{x}_S^n(\mathbf{A}^H (\mathbf{y} + \delta))\| \leq C_n \|\delta\|, \quad (9)$$

where $C_n = \alpha \|\mathbf{A}\|_2 \left(\frac{1 - \left(\frac{M\alpha}{\sqrt{2\pi}\sigma}\right)^n}{1 - \frac{M\alpha}{\sqrt{2\pi}\sigma}} \right) + \|\mathbf{A}\|_2 \left(\frac{M\alpha}{\sqrt{2\pi}\sigma}\right)^n$, with $\alpha = \|(\mathbf{A}^H \mathbf{A} + \mathbf{I})^{-1}\|_2$ and $M = 2 \max_{\mathbf{x}} (\|\mathcal{D}_\theta(\mathbf{x})\|)$.

The proof is provided in the Appendix. Note that the output of SMUG $\mathbf{x}_S^n(\cdot)$ depends on both the initial input (here $\mathbf{A}^H \mathbf{y}$) and the measurements \mathbf{y} . We abbreviated it to $\mathbf{x}_S^n(\mathbf{A}^H \mathbf{y})$ in the theorem and proof for notational simplicity. The constant C_n depends on the number of iterations or unrolling steps n as well as the RS standard deviation parameter σ . For large σ , the robustness error bound for SMUG clearly decreases as the number of iterations n increases. In particular, if $\sigma > M\alpha/\sqrt{2\pi}$, then as $n \rightarrow \infty$, $C_n \rightarrow \alpha \|\mathbf{A}\|_2 / \left(1 - \frac{M\alpha}{\sqrt{2\pi}\sigma}\right)$. Furthermore, as $\sigma \rightarrow \infty$, $C_n \rightarrow C \triangleq \alpha \|\mathbf{A}\|_2$. Clearly, if $\alpha \leq 1$ and $\|\mathbf{A}\|_2 \leq 1$ (normalized), then $C \leq 1$. Thus, for sufficient smoothing, the error introduced in the SMUG output due to input perturbation never gets worse than the size of the input perturbation. Thus, the output is stable with respect to perturbations. These results corroborate experimental results in Section IV on how SMUG is robust (whereas other methods, such as vanilla MODL, breakdown) when increasing the number of unrolling steps at test time, and is also more robust for larger σ (with good accuracy-robustness trade-off).

The only assumption in our analysis is that the denoiser network output is bounded in norm. This consideration is handled readily when the denoiser network incorporates bounded activation functions such as the sigmoid or hyperbolic tangent. Alternatively, if we expect image intensities to lie within a certain range, a simple clipping operation in the network output would ensure boundedness for the analysis.

A key distinction between SMUG and prior works, such as RS-E2E [28], is that smoothing is performed in every iteration. Moreover, while [28] assumes the end-to-end mapping is bounded, in MODL or SMUG, it clearly isn't because the data-consistency step's output is unbounded as y grows.

D. Solution to (Q4): Weighted Smoothing

In this subsection, we present a modified formulation of randomized smoothing to improve its performance in SMUG. Randomized smoothing in practice involves uniformly averaging images denoised with random perturbations. This can be viewed as a type of mean filter, which leads to oversmoothing of structural information in practice. As such, we propose weighted randomized smoothing, which employs an encoder to assess a weighting (scalar) for each denoised image and subsequently applies the optimal weightings while aggregating images to enhance the reconstruction performance. Our method not only surpasses the SMUG technique but also excels in enhancing image sharpness across various types of perturbation sources. This allows for a more versatile or flexible and effective approach for improving image quality under different conditions.

The weighted randomized smoothing operation applied on a function $f(\cdot)$ is as follows:

$$g_w(\mathbf{x}) := \frac{\mathbb{E}_\eta[w(\mathbf{x} + \boldsymbol{\eta})f(\mathbf{x} + \boldsymbol{\eta})]}{\mathbb{E}_\eta[w(\mathbf{x} + \boldsymbol{\eta})]}, \quad (10)$$

where $w(\cdot)$ is an input-dependent weighting function.

Based on the weighted smoothing operation in (10), we introduce **Weighted SMUG**. This approach involves the application of weighted RS at each denoising step, and the weighting encoder is trained in conjunction with the denoiser during the fine-tuning stage. Specifically, in the n -th unrolling step, we use a weighting encoder \mathcal{E}_ϕ , parameterized by ϕ , to learn the weight of each image used for (weighted) averaging. Here, we use \mathbf{x}_W^n to denote the output of the n -th block. Initializing $\mathbf{x}_W^0 = \mathbf{A}^H \mathbf{y}$, the output of Weighted SMUG w.r.t. n is

$$\begin{aligned} \mathbf{x}_W^{n+1} &= \arg \min_{\mathbf{x}} \|\mathbf{A}\mathbf{x} - \mathbf{y}\|_2^2 + \\ &\lambda \left\| \mathbf{x} - \frac{\mathbb{E}_\eta[\mathcal{E}_\phi(\mathbf{x}_W^n + \boldsymbol{\eta})\mathcal{D}_\theta(\mathbf{x}_W^n + \boldsymbol{\eta})]}{\mathbb{E}_\eta[\mathcal{E}_\phi(\mathbf{x}_W^n + \boldsymbol{\eta})]} \right\|_2^2. \end{aligned} \quad (11)$$

After N iterations, the final output of Weighted SMUG is $\mathbf{x}_W^N = \mathbf{F}_{\text{wSMUG}}(\mathbf{x}^0)$. Figure 4 illustrates the architecture of weighted SMUG.

Furthermore, we extend the ‘‘pre-training + fine-tuning’’ approach proposed in Section III-B to the Weighted SMUG method. In this case, we obtain the **fine-tuned** $\boldsymbol{\theta}$ and ϕ by using

$$\min_{\boldsymbol{\theta}, \phi} \mathbb{E}_{(\mathbf{y}, \mathbf{t})} [\lambda_l \|\mathbf{F}_{\text{wSMUG}}(\mathbf{A}^H \mathbf{y}) - \mathbf{t}\|_2^2 + \ell_{\text{UStab}}(\boldsymbol{\theta}; \mathbf{y}, \mathbf{t})]. \quad (12)$$

IV. EXPERIMENTS

A. Experimental Setup

Models & datasets: We evaluate the performance of the proposed methods, SMUG and Weighted SMUG, and compare the results with other schemes such as the RS-E2E method. We use the `fastMRI` dataset including brain and knee scans [35]. For the MoDL architecture, we use the recent state-of-the-art denoising network Deep iterative Down Network, which consists of 3 down-up blocks (DUBs) and 64 channels [38]. Additionally, for MODL, we use $N = 8$ unrolling steps with denoising regularization parameter $\lambda = 1$. The conjugate gradient method [32], with a tolerance level of 10^{-6} , is utilized to execute the DC block. We use binary Cartesian k-space undersampling masks which correspond to 4x (25.0% sampling) and 8x (12.5% sampling) acceleration of the k-space acquisition. The coil sensitivity maps for all scenarios were generated with the BART toolbox [39].

Training: For our study, we execute two experimental cases. For the first case, we utilize the `fastMRI` knee dataset, with 32 images for validation and 64 unseen images for testing. In the second case, we employ our method for the `fastMRI` brain dataset. We used 3000 training scans in both cases. We use a batch size of 2 and 60 training epochs. The experiments are run using two A5000 GPUs. The ADAM optimizer [40] is utilized for training the network weights with momentum parameters of (0.5, 0.999) and learning rate of 10^{-4} . The stability parameter λ_ℓ in (8) (and (12)) is tuned so that the standard accuracy of the learned model is comparable to vanilla MODL. For RS-E2E, we set the standard deviation of Gaussian noise to $\sigma = 0.01$, and use 10 Monte Carlo samplings to implement the smoothing operation. Note that in our experiments, Gaussian noise and corruptions are added to real and imaginary parts of the data with the indicated σ .

Testing: We evaluate our methods on clean data (without additional perturbations), data with randomly injected noise, and data contaminated with worst-case additive perturbations. The worst-case disturbances allow us to see worst-case method sensitivity and are generated by the ℓ_∞ -norm based PGD scheme with 10 steps [20] corresponding to $\|\boldsymbol{\delta}\|_\infty \leq \epsilon$, where ϵ is set nominally as the maximum underlying k-space real and imaginary part magnitude scaled by 0.05. We will only indicate the scaling factor for ϵ (e.g., 0.05) in the results and plots that follow. The quality of reconstructed images is measured using peak signal-to-noise ratio (PSNR) and structure similarity index measure (SSIM) [41]. In addition to the worst-case perturbations and random noise, we evaluate the performance of our methods in the presence of additional instability sources such as (i) different undersampling rates, and (ii) different numbers of unrolling steps.

We have also observed the performance of adversarial training. While it provides consistent performance when handling worst-case additive perturbations at test time, we observed that its effectiveness degraded for other perturbations including modified sampling rates and varied unrolling steps. Moreover, adversarial training is much slower than SMUG. Importantly, the proposed SMUG and Weighted SMUG are not trained to

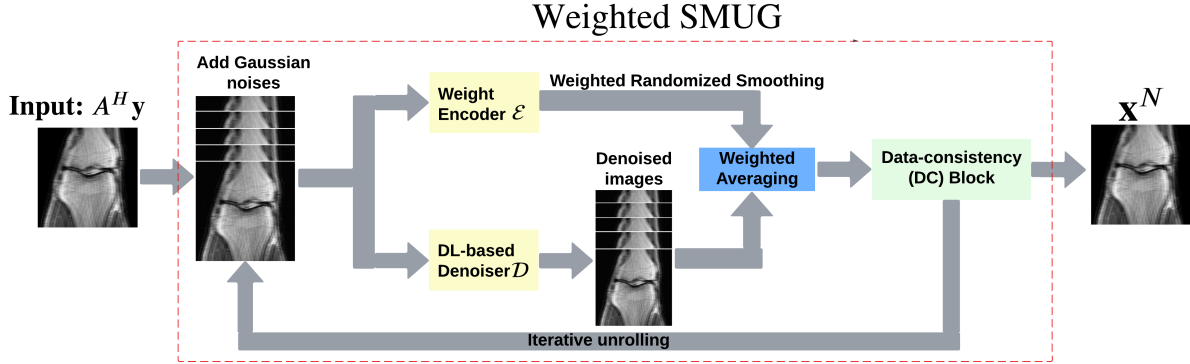


Fig. 4: Architecture of weighted SMUG.

be robust to any specific perturbations or instabilities, but are nevertheless effective for many such scenarios.

B. Results

Table I presents PSNR and SSIM values for different smoothing architectures with different training schemes, along with vanilla MODL as a baseline using the brain dataset. The evaluation is conducted on the clean, noisy (with added Gaussian noise), and worst-case perturbed (using PGD for each method) measurements. As indicated by the PSNR and SSIM values, we observe that our method, SMUG, outperforms RS-E2E and vanilla MODL in robust accuracy, i.e., image quality with perturbations. This observation is consistent with the visualization of reconstructed images for the brain dataset in **Fig. 5**. Furthermore, we observe that Weighted SMUG outperforms SMUG in robustness. However, weighted SMUG requires longer time for training, which represents a trade-off. The clean accuracies of Weighted SMUG and SMUG are similar to vanilla MoDL indicating a good clean accuracy vs. robustness trade-off.

Table II compares image reconstruction quality with different methods at two sampling acceleration factors for the knee dataset. We observe quite similar and congruous outcomes to those reported in Table I. **Figs. 6** and **7** show reconstructed images by different methods for knee scans at 4x and 8x undersampling, respectively. We observe that SMUG and Weighted SMUG show fewer artifacts, sharper features, and fewer errors when compared to Vanilla MoDL reconstruction in the presence of the worst-case perturbations.

Fig. 8 presents PSNR results for the considered models under different scales of worst-case perturbations (i.e., attack strength ϵ). We used the knee dataset for this and following results. We observe that SMUG and weighted SMUG outperform other methods across perturbation strengths.

Next, we evaluate the effectiveness of the proposed MRI reconstruction methods when faced with sampling rates and unrolling steps that are different from the settings used in the training phase. **Figs. 9** and **10** present the evaluation results of SMUG and Weighted SMUG along with the two baselines, vanilla MODL, and RS-E2E. As observed, SMUG and Weighted SMUG achieve remarkable improvements in robustness with different sampling rates and unrolling steps, which MODL and RS-E2E fail to achieve. Although we do not intentionally design our method to mitigate MODL's

instabilities against different sampling rates and unrolling steps, the SMUG approaches nevertheless provide improved PSNRs over other baselines. This indicates broader value for the robustification strategies incorporated in our schemes.

We conduct additional studies on the unrolled stability loss in our scheme to show the importance of integrating target image denoising into SMUG's training pipeline in (7). **Fig. 13** presents PSNR values versus perturbation strength/scaling (ϵ) when using different alternatives to $\mathcal{D}_\theta(t)$ in (7), including t (the original target image), $\mathcal{D}_\theta(x_n)$ (denoised output of each unrolling step), and variants when using the fixed, vanilla MODL's denoiser $\mathcal{D}_{\theta_{\text{MoDL}}}$ instead. As we can see, the performance of SMUG varies when the UStab loss (7) is configured differently. The proposed $\mathcal{D}_\theta(t)$ outperforms other baselines. A possible reason is that it infuses supervision of target images in an adaptive, denoising-friendly manner, i.e., taking the influence of \mathcal{D}_θ into consideration.

To comprehensively assess the influence of the introduced noise during smoothing, denoted as η , on the efficacy of the suggested approaches, we undertake an experiment involving varying noise standard deviations σ . The outcomes, documented in terms of RMSE, are showcased in **Fig. 11**. The accuracy (reconstruction quality w.r.t. ground truth) and robustness error (error between with and without measurement perturbation cases) are shown for both SMUG and RS-E2E. We notice a notable trend: as the noise level σ increases, the accuracy for both methods improves before beginning to degrade. Importantly, SMUG consistently outperforms end-to-end smoothing. Furthermore, the robustness error continually drops as σ increases (corroborating with our analysis/bound in Section III), with more rapid decrease for SMUG.

In our final study, we analyze the behavior of the Weighted SMUG algorithm. We delve into the nuances of weighted smoothing, which can assign different weights to different images during the smoothing process. The aim is to gauge how the superior performance of Weighted SMUG arises from the variations in learned weights. Our findings indicate that among the 10 Monte Carlo samplings implemented for the smoothing operation, those with lower denoising RMSE when compared to the ground truth images generally receive higher weights, as illustrated in **Fig. 12**.

TABLE I: Performance comparison of different smoothing architectures (RS-E2E, SMUG, Weighted SMUG), together with vanilla MODL at 4x undersampling. Here, ‘Clean Accuracy’, ‘Robust Accuracy by random noise’, and ‘Robust Accuracy by PGD’ refer to PSNR/SSIM evaluated on benign data, random noise-injected (with Gaussian noise) data, and PGD-enabled worst-case perturbed data, respectively. \uparrow signifies that a higher number indicates a better reconstruction accuracy. The result $a\pm b$ represents mean a and standard deviation b over 64 testing brain Fast MRI images. The relative (better or worse) performance of methods w.r.t. metric a is reported with respect to that of vanilla MODL.

| Models Metrics | Clean Accuracy | | Robust Accuracy by random noise | | Robust Accuracy by PGD | |
|----------------------|-------------------------|--------------------------|---------------------------------|-------------------------|------------------------|--------------------------|
| | PSNR \uparrow | SSIM \uparrow | PSNR \uparrow | SSIM \uparrow | PSNR \uparrow | SSIM \uparrow |
| Vanilla MoDL | 32.7 \pm 2.87 | 0.921 \pm 0.07 | 31.77 \pm 2.77 | 0.908 \pm 0.07 | 24.45 \pm 2.42 | 0.767 \pm 0.07 |
| RS-E2E | -0.03 \pm 3.24 | -0.001 \pm 0.07 | +0.43 \pm 2.90 | +0.010 \pm 0.07 | +0.86 \pm 2.70 | +0.008 \pm 0.08 |
| SMUG (Ours) | -0.05 \pm 3.01 | -0.001 \pm 0.08 | +0.75 \pm 2.98 | +0.015 \pm 0.08 | +3.98 \pm 2.28 | +0.014 \pm 0.11 |
| Weighted SMUG (Ours) | -0.06 \pm 2.25 | -0.001 \pm 0.07 | +0.87 \pm 2.97 | +0.02 \pm 0.08 | +4.82 \pm 2.2 | +0.034 \pm 0.09 |

TABLE II: Similar setup as Table I, but the training is with knee dataset images, which include 4x and 8x k-space undersampling and testing on knee dataset images with the same undersampling rate for the comparisons.

| Ax Factor | Models Metrics | Clean Accuracy | | Robust Accuracy by random noise | | Robust Accuracy by PGD | |
|-----------|----------------------|------------------|--------------------|---------------------------------|--------------------------|-------------------------|--------------------------|
| | | PSNR \uparrow | SSIM \uparrow | PSNR \uparrow | SSIM \uparrow | PSNR \uparrow | SSIM \uparrow |
| 4x | Vanilla MoDL | 31.82 \pm 2.44 | 0.918 \pm 0.08 | 30.67 \pm 2.06 | 0.91 \pm 0.09 | 24.23 \pm 1.82 | 0.764 \pm 0.08 |
| | RS-E2E | -0.04 \pm 2.37 | -0.002 \pm 0.08 | +0.48 \pm 2.31 | +0.01 \pm 0.07 | +2.07 \pm 2.17 | +0.012 \pm 0.08 |
| | SMUG (Ours) | -0.06 \pm 2.23 | -0.0039 \pm 0.09 | +0.72 \pm 2.32 | +0.018 \pm 0.08 | +4.31 \pm 2.22 | +0.027 \pm 0.07 |
| | Weighted SMUG (Ours) | -0.07 \pm 2.26 | -0.0041 \pm 0.11 | +0.82 \pm 2.34 | +0.03 \pm 0.10 | +4.67 \pm 2.25 | +0.029 \pm 0.10 |
| 8x | Vanilla MoDL | 30.83 \pm 3.14 | 0.905 \pm 0.10 | 28.76 \pm 2.87 | 0.872 \pm 0.09 | 21.28 \pm 2.54 | 0.712 \pm 0.10 |
| | RS-E2E | -0.06 \pm 3.08 | -0.002 \pm 0.11 | +0.54 \pm 2.91 | +0.017 \pm 0.09 | +1.97 \pm 2.74 | +0.011 \pm 0.09 |
| | SMUG (Ours) | -0.09 \pm 3.04 | -0.019 \pm 0.12 | +0.79 \pm 2.92 | +0.021 \pm 0.09 | +4.84 \pm 2.44 | +0.03 \pm 0.08 |
| | Weighted SMUG (Ours) | -0.08 \pm 3.02 | -0.021 \pm 0.10 | +0.94 \pm 2.93 | +0.024 \pm 0.08 | +5.32 \pm 2.48 | +0.033 \pm 0.09 |

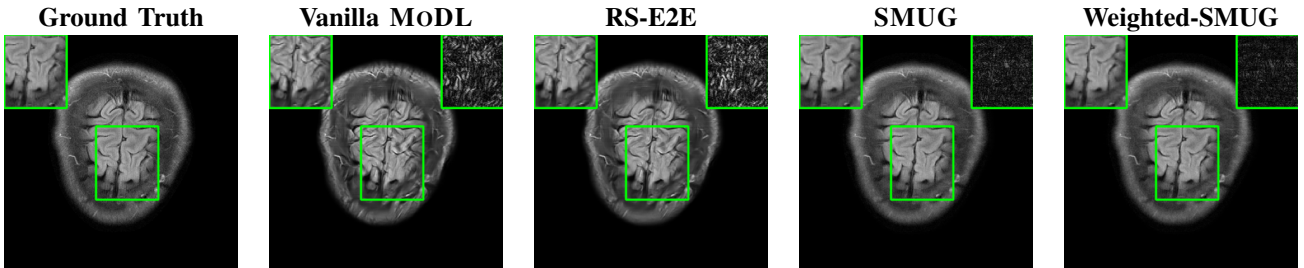


Fig. 5: Visualization of ground truth and reconstructed images using different methods for 4x k-space undersampling, evaluated on PGD-generated worst-case inputs of perturbation strength $\epsilon = 0.02$.



Fig. 6: Visualization of ground-truth and reconstructed images using different methods for 4x k-space undersampling, evaluated on PGD-generated worst-case inputs of perturbation strength $\epsilon = 0.02$.

V. DISCUSSION AND CONCLUSION

In this work, we proposed a scheme for improving the robustness of DL-based MRI reconstruction. In particular, we investigated deep unrolled reconstruction’s weaknesses in robustness against worst-case or noise-like additive perturbations, sampling rates, and unrolling steps. To improve the robustness of the unrolled scheme, we proposed SMUG with a

novel unrolled smoothing loss. We also provided a theoretical analysis on the robustness achieved by our proposed method. Compared to the vanilla MODL approach and other schemes, we empirically showed that our approach is effective and can significantly improve the robustness of a deep unrolled scheme against a diverse set of external perturbations. We also further improved SMUG’s robustness by introducing

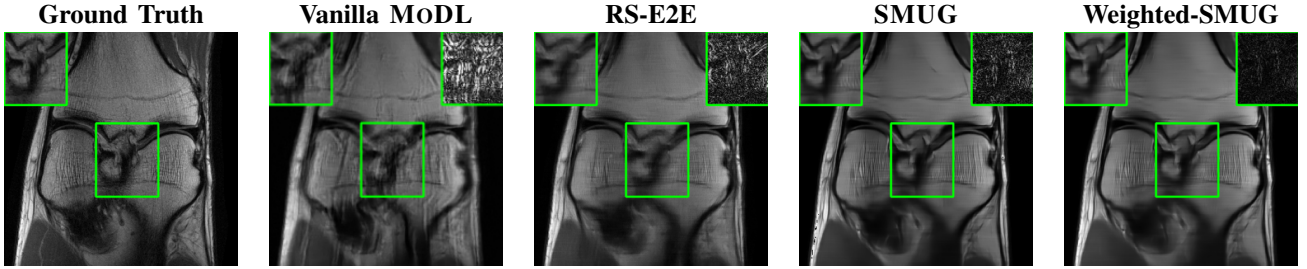


Fig. 7: Visualization of ground truth and reconstructed images using different methods for 8x k-space undersampling, evaluated on PGD-generated worst-case inputs of perturbation scaling $\epsilon = 0.02$.

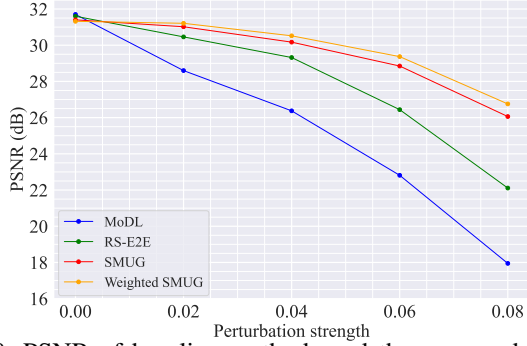


Fig. 8: PSNR of baseline methods and the proposed method versus perturbation strength (i.e., scaling) ϵ used in PGD-generated worst-case examples at testing time with 4x k-space undersampling. $\epsilon = 0$ corresponds to clean accuracy.

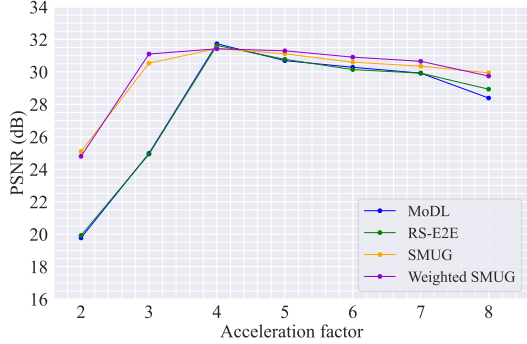


Fig. 9: PSNR results for different MRI reconstruction methods versus different measurement sampling rates (models trained at 4x acceleration).

weighted smoothing as an alternative to conventional RS, which adaptively weights different images when aggregating them. In future work, we hope to apply the proposed schemes to other imaging modalities and evaluate robustness against more types of realistic perturbations.

APPENDIX A PROOF OF THEOREM 1

A. Preliminary of Theorem 1

Lemma 1. Let $f : \mathbb{R}^d \rightarrow \mathbb{R}^m$ be any bounded function. Let $\eta \sim \mathcal{N}(0, \sigma^2 \mathbf{I})$. We define $g : \mathbb{R}^d \rightarrow \mathbb{R}^m$ as

$$g(\mathbf{x}) = \mathbb{E}_{\eta}[f(\mathbf{x} + \eta)].$$

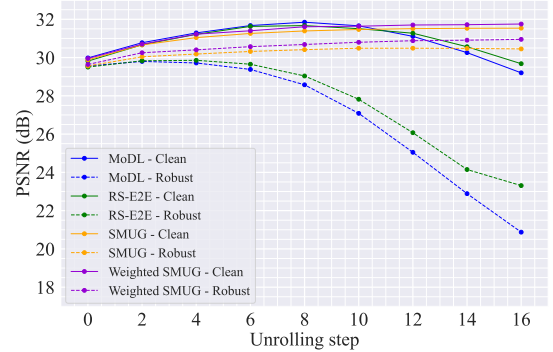


Fig. 10: PSNR results for different MRI reconstruction methods at 4x k-space undersampling versus number of unrolling steps (8 steps used in training). “Clean” and “Robust” denote the cases without and with added worst-case (for each method) measurement perturbations.

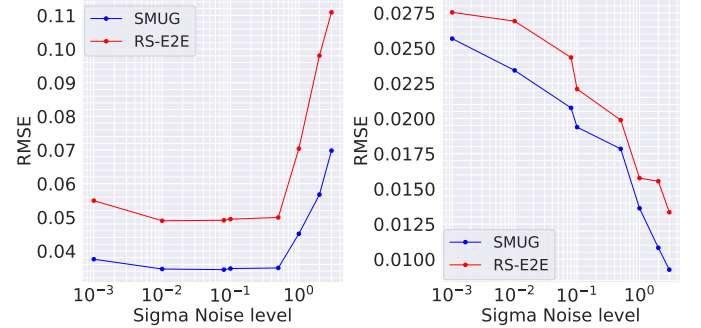


Fig. 11: Left: Norm of difference between SMUG and RS-E2E reconstructions and the ground truth for different choices of σ in the smoothing process. A worst-case PGD perturbation δ computed at $\sigma = 0.01$ was added to the measurements in all cases. Right: Robustness error for SMUG and RS-E2E at various σ , i.e., norm of difference between output with the perturbation δ and without it.

Then, g is an $\frac{M}{\sqrt{2\pi}\sigma}$ -Lipschitz map, where $M = 2 \max_{\mathbf{x} \in \mathbb{R}^d} (\|f(\mathbf{x})\|_2)$. In particular, for any $\mathbf{x}, \delta \in \mathbb{R}^d$:

$$\|g(\mathbf{x}) - g(\mathbf{x} + \delta)\|_2 \leq \frac{M}{\sqrt{2\pi}\sigma} \|\delta\|_2.$$

Proof. The proof of this bound follows recent work [28], with a modification on M . Let μ be the probability distribution function of random variable η . By the change of variables $\mathbf{w} = \mathbf{x} + \eta$ and $\mathbf{w} = \mathbf{x} + \eta + \delta$ for the integrals constituting $g(\mathbf{x})$ and

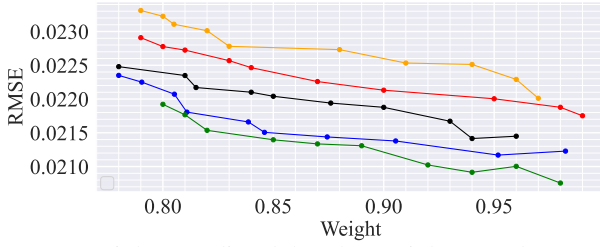


Fig. 12: Weights predicted by the weight encoder network in Weighted SMUG (from final layer of unrolling) plotted against root mean squared error (RMSE) of the corresponding denoised images for 5 randomly selected scans (with 4x undersampling).

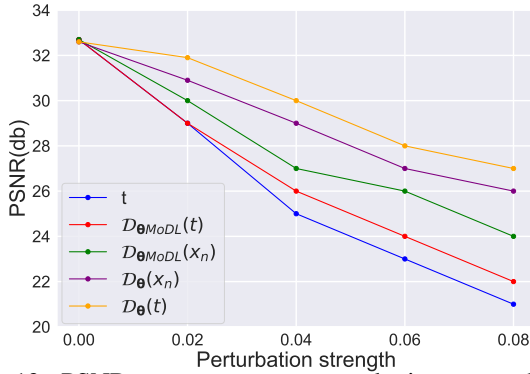


Fig. 13: PSNR vs. worst-case perturbation strength (ϵ) for SMUG for different configurations of UStab loss (7).

$g(\mathbf{x} + \delta)$, we have $\|g(\mathbf{x}) - g(\mathbf{x} + \delta)\|_2 = \|\int_{\mathbb{R}^d} f(\mathbf{w})[\mu(\mathbf{w} - \mathbf{x}) - \mu(\mathbf{w} - \mathbf{x} - \delta)] d\mathbf{w}\|_2$. Then, we have $\|g(\mathbf{x}) - g(\mathbf{x} + \delta)\|_2$

$$\leq \int_{\mathbb{R}^d} \|f(\mathbf{w})[\mu(\mathbf{w} - \mathbf{x}) - \mu(\mathbf{w} - \mathbf{x} - \delta)]\|_2 d\mathbf{w},$$

which is a standard result for the norm of an integral. We further apply Holder's inequality to upper bound $\|g(\mathbf{x}) - g(\mathbf{x} + \delta)\|_2$ with

$$\max_{\mathbf{x} \in \mathbb{R}^d} (\|f(\mathbf{x})\|_2) \int_{\mathbb{R}^d} |\mu(\mathbf{w} - \mathbf{x}) - \mu(\mathbf{w} - \mathbf{x} - \delta)| d\mathbf{w}. \quad (13)$$

Observe that $\mu(\mathbf{w} - \mathbf{x}) \geq \mu(\mathbf{w} - \mathbf{x} - \delta)$ if $\|\mathbf{w} - \mathbf{x}\|_2 \leq \|\mathbf{w} - \mathbf{x} - \delta\|_2$. Let $D = \{\mathbf{w} : \|\mathbf{w} - \mathbf{x}\|_2 \leq \|\mathbf{w} - \mathbf{x} - \delta\|_2\}$. Then, we can rewrite the above bound as

$$= \max_{\mathbf{x} \in \mathbb{R}^d} (\|f(\mathbf{x})\|_2) \cdot 2 \int_D [\mu(\mathbf{w} - \mathbf{x}) - \mu(\mathbf{w} - \mathbf{x} - \delta)] d\mathbf{w} \quad (14)$$

$$= \frac{M}{2} (2 \int_D \mu(\mathbf{w} - \mathbf{x}) d\mathbf{w} - 2 \int_D \mu(\mathbf{w} - \mathbf{x} - \delta) d\mathbf{w}). \quad (15)$$

Following Lemma 3 in [42], we obtain the bound

$$2 \int_D \mu(\mathbf{w} - \mathbf{x}) d\mathbf{w} - 2 \int_D \mu(\mathbf{w} - \mathbf{x} - \delta) d\mathbf{w} \leq \frac{2}{\sqrt{2\pi\sigma}} \|\delta\|_2, \quad (16)$$

which implies that $\|g(\mathbf{x}) - g(\mathbf{x} + \delta)\|_2 \leq \frac{2 \max_{\mathbf{x} \in \mathbb{R}^d} (\|f(\mathbf{x})\|_2)}{\sqrt{2\pi\sigma}} \|\delta\|_2 = \frac{M}{\sqrt{2\pi\sigma}} \|\delta\|_2$. This completes the proof. \square

B. Proof of Theorem 1

Proof. Assume that the data consistency step in MoDL at iteration n is denoted by $\mathbf{x}_M^n(\mathbf{A}^H \mathbf{y})$. We will sometimes drop the input and \mathbf{y} dependence for notational simplicity. Then

$$\mathbf{x}_M^1 = (\mathbf{A}^H \mathbf{A} + \mathbf{I})^{-1} (\mathbf{A}^H \mathbf{y} + \mathcal{D}_\theta(\mathbf{A}^H \mathbf{y})), \quad (17)$$

$$\mathbf{x}_M^n = (\mathbf{A}^H \mathbf{A} + \mathbf{I})^{-1} (\mathbf{A}^H \mathbf{y} + \mathcal{D}_\theta(\mathbf{x}_M^{n-1})), \quad (18)$$

where \mathcal{D}_θ is the denoiser function. For the sake of simplicity and consistency with the experiments, we use the weighting parameter $\lambda = 1$ (in the data consistency step). We note that the proof works for arbitrary λ . SMUG introduces an iteration-wise smoothing step into MoDL as follows:

$$\mathbf{x}_S^1 = ((\mathbf{A}^H \mathbf{A} + \mathbf{I})^{-1} (\mathbf{A}^H \mathbf{y} + \mathbb{E}_{\eta_1}[\mathcal{D}_\theta(\mathbf{A}^H \mathbf{y} + \eta_1)])) \quad (19)$$

$$\mathbf{x}_S^n = ((\mathbf{A}^H \mathbf{A} + \mathbf{I})^{-1} (\mathbf{A}^H \mathbf{y} + \mathbb{E}_{\eta_n}[\mathcal{D}_\theta(\mathbf{x}_S^{n-1} + \eta_n)])) \quad (20)$$

$$= (\mathbf{A}^H \mathbf{A} + \mathbf{I})^{-1} (\mathbf{A}^H \mathbf{y} + \mathbb{E}_{\eta_n}[\mathcal{D}_\theta(\mathbf{x}_S^{n-1} + \eta_n)]), \quad (21)$$

where we apply the expectation to the denoiser \mathcal{D}_θ at each iteration. We use η_n to denote the noise during smoothing at iteration n . The robustness error of SMUG after n iterations is $\|\mathbf{x}_S^n(\mathbf{A}^H \mathbf{y}) - \mathbf{x}_S^n(\mathbf{A}^H(\mathbf{y} + \delta))\|$. We apply Lemma 1 and properties of the norm (e.g., triangle inequality) to bound $\|\mathbf{x}_S^n(\mathbf{A}^H \mathbf{y}) - \mathbf{x}_S^n(\mathbf{A}^H(\mathbf{y} + \delta))\|$ as

$$\begin{aligned} &\leq \|(\mathbf{A}^H \mathbf{A} + \mathbf{I})^{-1} \mathbf{A}^H \delta\| \quad (22) \\ &+ \|(\mathbf{A}^H \mathbf{A} + \mathbf{I})^{-1} \cdot (\mathbb{E}_{\eta_n}[\mathcal{D}_\theta(\mathbf{x}_S^{n-1}(\mathbf{A}^H \mathbf{y}) + \eta_n)] - \mathbb{E}_{\eta_n}[\mathcal{D}_\theta(\mathbf{x}_S^{n-1}(\mathbf{A}^H(\mathbf{y} + \delta)) + \eta_n)])\| \\ &\leq \|(\mathbf{A}^H \mathbf{A} + \mathbf{I})^{-1}\|_2 \|\mathbf{A}^H \delta\|_2 \\ &+ \|(\mathbf{A}^H \mathbf{A} + \mathbf{I})^{-1}\|_2 \|\mathbb{E}_{\eta_n}[\mathcal{D}_\theta(\mathbf{x}_S^{n-1}(\mathbf{A}^H \mathbf{y}) + \eta_n)] - \mathbb{E}_{\eta_n}[\mathcal{D}_\theta(\mathbf{x}_S^{n-1}(\mathbf{A}^H(\mathbf{y} + \delta)) + \eta_n)]\| \\ &\leq \|(\mathbf{A}^H \mathbf{A} + \mathbf{I})^{-1}\|_2 \|\mathbf{A}^H \delta\|_2 + \|(\mathbf{A}^H \mathbf{A} + \mathbf{I})^{-1}\|_2 \times \quad (23) \\ &\left(\frac{M}{\sqrt{2\pi\sigma}}\right) \|\mathbf{x}_S^{n-1}(\mathbf{A}^H \mathbf{y}) - \mathbf{x}_S^{n-1}(\mathbf{A}^H(\mathbf{y} + \delta))\|. \end{aligned}$$

Here, $M = 2 \max_{\mathbf{x}} (\|\mathcal{D}_\theta(\mathbf{x})\|)$. Then we plug in the expressions for $\mathbf{x}_S^{n-1}(\mathbf{A}^H \mathbf{y})$ and $\mathbf{x}_S^{n-1}(\mathbf{A}^H(\mathbf{y} + \delta))$ (from (20)) and bound their normed difference with $\|(\mathbf{A}^H \mathbf{A} + \mathbf{I})^{-1} \mathbf{A}^H \delta\| + \|(\mathbf{A}^H \mathbf{A} + \mathbf{I})^{-1} \cdot (\mathbb{E}_{\eta_{n-1}}[\mathcal{D}_\theta(\mathbf{x}_S^{n-2}(\mathbf{A}^H \mathbf{y}) + \eta_{n-1})] - \mathbb{E}_{\eta_{n-1}}[\mathcal{D}_\theta(\mathbf{x}_S^{n-2}(\mathbf{A}^H(\mathbf{y} + \delta)) + \eta_{n-1})])\|$. This is bounded above similarly as for (22). We repeat this process until we reach the initial \mathbf{x}_S^0 on the right hand side. This yields the following bound involving a geometric series.

$$\|\mathbf{x}_S^n(\mathbf{A}^H \mathbf{y}) - \mathbf{x}_S^n(\mathbf{A}^H(\mathbf{y} + \delta))\| \quad (24)$$

$$\leq \|\mathbf{A}^H \delta\|_2 \left(\sum_{j=1}^n \|(\mathbf{A}^H \mathbf{A} + \mathbf{I})^{-1}\|_2^j \cdot \left(\frac{M}{\sqrt{2\pi\sigma}}\right)^{j-1} \right) + \|(\mathbf{A}^H \mathbf{A} + \mathbf{I})^{-1}\|_2^n \left(\frac{M}{\sqrt{2\pi\sigma}}\right)^n \|\mathbf{A}^H \delta\|_2 \quad (25)$$

$$\leq \|\mathbf{A}\|_2 \|\delta\|_2 \|(\mathbf{A}^H \mathbf{A} + \mathbf{I})^{-1}\|_2 \left(\frac{1 - \left(\frac{M}{\sqrt{2\pi\sigma}}\right)^n \|(\mathbf{A}^H \mathbf{A} + \mathbf{I})^{-1}\|_2^n}{1 - \frac{M}{\sqrt{2\pi\sigma}} \|(\mathbf{A}^H \mathbf{A} + \mathbf{I})^{-1}\|_2} \right) + \|(\mathbf{A}^H \mathbf{A} + \mathbf{I})^{-1}\|_2^n \left(\frac{M}{\sqrt{2\pi\sigma}}\right)^n \|\mathbf{A}\|_2 \|\delta\|_2 \leq C_n \|\delta\|_2, \quad (26)$$

where we used the geometric series formula, and $C_n = \alpha \|\mathbf{A}\|_2 \left(\frac{1 - \left(\frac{M\alpha}{\sqrt{2\pi\sigma}}\right)^n}{1 - \frac{M\alpha}{\sqrt{2\pi\sigma}}} \right) + \|\mathbf{A}\|_2 \left(\frac{M\alpha}{\sqrt{2\pi\sigma}}\right)^n$, with $\alpha = \|(\mathbf{A}^H \mathbf{A} + \mathbf{I})^{-1}\|_2$. \square

REFERENCES

- [1] M. Lustig, D. L. Donoho, et al., “Compressed Sensing MRI,” *IEEE signal processing magazine*, 2008.
- [2] M. Kivanc Miheci, I. Kozintsev, K. Ramchandran, and P. Moulin, “Low-complexity image denoising based on statistical modeling of wavelet coefficients,” *IEEE Signal Processing Letters*, vol. 6, no. 12, pp. 300–303, 1999.
- [3] S. Ma, W. Yin, Y. Zhang, and A. Chakraborty, “An efficient algorithm for compressed MR imaging using total variation and wavelets,” in *2008 IEEE Conference on Computer Vision and Pattern Recognition*, 2008, pp. 1–8.
- [4] S. Ravishanker and Y. Bresler, “MR image reconstruction from highly undersampled k-space data by dictionary learning,” *IEEE Transactions on Medical Imaging*, vol. 30, no. 5, pp. 1028–1041, 2011.
- [5] S. G. Lingala and M. Jacob, “Blind compressive sensing dynamic MRI,” *IEEE Transactions on Medical Imaging*, vol. 32, no. 6, pp. 1132–1145, 2013.
- [6] S. Ravishanker and Y. Bresler, “Learning sparsifying transforms,” *IEEE Transactions on Signal Processing*, vol. 61, no. 5, pp. 1072–1086, 2012.
- [7] S. Ravishanker, J. C. Ye, and J. A. Fessler, “Image reconstruction: From sparsity to data-adaptive methods and machine learning,” *Proceedings of the IEEE*, vol. 108, no. 1, pp. 86–109, 2020.
- [8] Ravishanker, B. Wen, and S. Pfister, L. and Bresler Y., “Transform learning for magnetic resonance image reconstruction: From model-based learning to building neural networks,” *IEEE Signal Processing Magazine*, vol. 37, no. 1, pp. 41–53, 2020.
- [9] J. Schlemper, C. Qin, J. Duan, R. M. Summers, and K. Hammernik, “Sigma-net: Ensembled iterative deep neural networks for accelerated parallel MR image reconstruction,” *arXiv preprint arXiv:1912.05480*, 2019.
- [10] S. Ravishanker, A. Lahiri, C. Blocker, and J. A. Fessler, “Deep dictionary-transform learning for image reconstruction,” in *2018 IEEE 15th International Symposium on Biomedical Imaging (ISBI 2018)*. IEEE, 2018, pp. 1208–1212.
- [11] H. K. Aggarwal, M. P. Mani, and M. Jacob, “Modl: Model-based deep learning architecture for inverse problems,” *IEEE transactions on medical imaging*, vol. 38, no. 2, pp. 394–405, 2018.
- [12] J. Schlemper, J. Caballero, J. V. Hajnal, A. N. Price, and D. Rueckert, “A deep cascade of convolutional neural networks for dynamic MR image reconstruction,” *IEEE Trans. Med. Imaging*, vol. 37, no. 2, pp. 491–503, Feb. 2018.
- [13] O. Ronneberger, P. Fischer, and T. Brox, “U-net: Convolutional networks for biomedical image segmentation,” in *Medical Image Computing and Computer-Assisted Intervention – MICCAI 2015*, 2015, pp. 234–241.
- [14] H. Zheng, F. Fang, and G. Zhang, “Cascaded dilated dense network with two-step data consistency for MRI reconstruction,” in *NeurIPS*, 2019.
- [15] J. Schlemper, J. Caballero, J. V. Hajnal, A. Price, and D. Rueckert, “A Deep Cascade of Convolutional Neural Networks for Dynamic MR Image Reconstruction,” *IEEE Transactions on Medical Imaging*, vol. 37, no. 2, pp. 491–503, 2018.
- [16] Y. Yang, J. Sun, H. Li, and Z. Xu, “Deep ADMM-Net for compressive sensing MRI,” in *Advances in Neural Information Processing Systems*, 2016, pp. 10–18.
- [17] K. Hammernik, T. Klatzer, E. Kobler, M. P. Recht, D. K. Sodickson, Thomas Pock, and Florian Knoll, “Learning a variational network for reconstruction of accelerated MRI data,” *Magnetic resonance in medicine*, vol. 79, no. 6, pp. 3055–3071, 2018.
- [18] Y. Romano, M. Elad, and P. Milanfar, “The Little Engine That Could: Regularization by Denoising (RED),” *SIAM Journal on Imaging Sciences*, vol. 10, no. 4, pp. 1804–1844, 2017.
- [19] G. T. Buzzard, S. H. Chan, S. Sreehari, and C. A. Bouman, “Plug-and-play unplugged: optimization-free reconstruction using consensus equilibrium,” *SIAM J. Imaging Sci.*, vol. 11, no. 3, pp. 2001–20, Jan. 2018.
- [20] V. Antun, F. Renna, C. Poon, B. Adcock, and A. C. Hansen, “On instabilities of deep learning in image reconstruction and the potential costs of AI,” *Proceedings of the National Academy of Sciences*, 2020.
- [21] C. Zhang, J. Jia, et al., “On Instabilities of Conventional Multi-Coil MRI Reconstruction to Small Adversarial Perturbations,” *arXiv preprint arXiv:2102.13066*, 2021.
- [22] D. Gilton, G. Ongie, and R. Willett, “Deep equilibrium architectures for inverse problems in imaging,” *IEEE Transactions on Computational Imaging*, vol. 7, pp. 1123–1133, 2021.
- [23] A. Madry, A. Makelov, L. Schmidt, D. Tsipras, and A. Vladu, “Towards deep learning models resistant to adversarial attacks,” *arXiv preprint arXiv:1706.06083*, 2017.
- [24] Y. Zhang, H. and Yu, J. Jiao, E. P. Xing, L. E. Ghaoui, and M. I. Jordan, “Theoretically principled trade-off between robustness and accuracy,” *International Conference on Machine Learning*, 2019.
- [25] J. Cohen, E. Rosenfeld, and Z. Kolter, “Certified adversarial robustness via randomized smoothing,” in *International Conference on Machine Learning*. PMLR, 2019, pp. 1310–1320.
- [26] H. Salman, M. Sun, G. Yang, A. Kapoor, and J. Z. Kolter, “Denoised smoothing: A provable defense for pretrained classifiers,” *Advances in Neural Information Processing Systems*, vol. 33, 2020.
- [27] Y. Zhang, Y. and Yao, J. Jia, J. Yi, M. Hong, S. Chang, and S. Liu, “How to robustify black-box ml models? a zeroth-order optimization perspective,” *arXiv preprint arXiv:2203.14195*, 2022.
- [28] A. Wolf, “Making medical image reconstruction adversarially robust,” 2019.
- [29] H. Liu, J. Jia, S. Liang, Y. Yao, S. Ravishanker, and S. Liu, “Smug: Towards robust mri reconstruction by smoothed unrolling,” 2023.
- [30] B. Zoph, G. Ghiasi, T. Lin, Y. Cui, H. Liu, E. D. Cubuk, and Q. Le, “Rethinking pre-training and self-training,” *Advances in Neural Information Processing Systems*, vol. 33, 2020.
- [31] D.L. Donoho, “Compressed sensing,” *IEEE Transactions on Information Theory*, vol. 52, no. 4, pp. 1289–1306, 2006.
- [32] H. K. Aggarwal, M. P. Mani, and M. Jacob, “MoDL: Model-based deep learning architecture for inverse problems,” *IEEE Trans. Med. Imaging*, vol. 38, no. 2, pp. 394–405, Feb. 2019.
- [33] Goodfellow I, Shlens, J. and Szegedy C, “Explaining and harnessing adversarial examples,” *2015 ICLR*, vol. arXiv preprint arXiv:1412.6572, 2015.
- [34] J. Jia, M. Hong, Y. Zhang, M. Akcakaya, and S. Liu, “On the robustness of deep learning-based MRI reconstruction to image transformations,” in *Workshop on Trustworthy and Socially Responsible Machine Learning, NeurIPS 2022*, 2022.
- [35] J. Zbontar, F. Knoll, A. Sriram, T. Murrell, Z. Huang, M. J. Muckley, A. Defazio, R. Stern, P. Johnson, M. Bruno, et al., “fastmri: An open dataset and benchmarks for accelerated mri,” *arXiv preprint arXiv:1811.08839*, 2018.
- [36] Y. Zhang, Y. Yao, J. Jia, J. Yi, M. Hong, S. Chang, and S. Liu, “How to robustify black-box ML models? a zeroth-order optimization perspective,” in *International Conference on Learning Representations*, 2022.
- [37] D.P. Kingma and J. Ba, “Adam: A method for stochastic optimization,” *2015 ICLR*, vol. arXiv preprint arXiv:1412.6980, 2015.
- [38] S. Yu, B. Park, and J. Jeong, “Deep iterative down-up cnn for image denoising,” in *Proceedings of the IEEE/CVF Conference on Computer Vision and Pattern Recognition Workshops*, 2019, pp. 0–0.
- [39] J. I. Tamir, F. Ong, J. Y. Cheng, M. Uecker, and M. Lustig, “Generalized magnetic resonance image reconstruction using the berkeley advanced reconstruction toolbox,” in *ISMRM Workshop on Data Sampling & Image Reconstruction, Sedona, AZ*, 2016.
- [40] D. P. Kingma and J. Ba, “Adam: A method for stochastic optimization,” *arXiv preprint arXiv:1412.6980*, 2014.
- [41] Z. Wang, A.C. Bovik, H.R. Sheikh, and P.E. Simoncelli, “Image quality assessment: From error visibility to structural similarity,” *IEEE Trans. Image Process.*, vol. 13, no. 4, pp. 600–612, 2004.
- [42] H. Lakshmanan, F. De, and P. Daniela, “Decentralized resource allocation in dynamic networks of agents,” *SIAM Journal on Optimization*, vol. 19, no. 2, pp. 911–940, 2008.